*Journal of Advanced Ceramics*
2022, **11**(12): 1849–1859
https://doi.org/10.1007/s40145-022-0651-x

ISSN 2226-4108
CN 10-1154/TQ

**Research Article**

# Taking advantage of Li-evaporation in $LiCoO_2$ as cathode for proton-conducting solid oxide fuel cells

Yangsen XU, Shoufu YU, Yanru YIN, Lei BI*

*School of Resource Environment and Safety Engineering, University of South China, Hengyang 421001, China*

Received: April 1, 2022; Revised: August 16, 2022; Accepted: August 23, 2022


**Abstract:** $LiCoO_2$, a widely used electrode material for Li-ion batteries, was found to be suitable as a cathode material for proton-conducting solid oxide fuel cells (H-SOFCs). Although the evaporation of Li in $LiCoO_2$ was detrimental to the Li-ion battery performance, the Li-evaporation was found to be beneficial for the H-SOFCs. The partial evaporation of Li in the $LiCoO_2$ material preparation procedure led to the *in-situ* formation of the $LiCoO_2$+$Co_3O_4$ composite. Compared to the cell using the pure phase $LiCoO_2$ cathode that only generated moderate fuel cell performance, the H-SOFCs using the $LiCoO_2$+$Co_3O_4$ cathode showed a high fuel cell performance of 1160 $mW \cdot cm^{-2}$ at 700 ℃, suggesting that the formation of $Co_3O_4$ was critical for enhancing the performance of the $LiCoO_2$ cathode. The first-principles calculation gave insights into the performance improvements, indicating that the *in-situ* formation of $Co_3O_4$ due to the Li-evaporation in $LiCoO_2$ could dramatically decrease the formation energy of oxygen vacancies that is essential for the high cathode performance. The evaporation of Li in $LiCoO_2$, which is regarded as a drawback for the Li-ion batteries, is demonstrated to be advantageous for the H-SOFCs, offering new selections of cathode candidates for the H-SOFCs.

**Keywords:** cathode; composite; proton conductor; solid oxide fuel cells (SOFCs)

## 1 Introduction

The current energy and environmental problems require the development of sustainable technologies and devices [1–5], and solid oxide fuel cells (SOFCs) that can convert chemical energies into electricity receive considerable attention [6]. The traditional SOFCs have to work at high temperatures (above 800 ℃), reducing the lifetime of the fuel cells [7,8]. Therefore, the development of the SOFCs working at lower temperatures (below 700 ℃) is highly desirable, and proton-conducting SOFCs (H-SOFCs) are proposed [9–11]. The H-SOFCs are able to work at low temperatures due to the high conductivity and low activation energy of the proton-conducting electrolytes [12–15]. However, the low working temperatures also result in slow cathode kinetics, making the development of cathodes a hot and important topic [16,17].

In the past decades, different cathode materials have been proposed for the H-SOFCs [18,19]. Although some of these cathode materials give good performance, none of them have been made into practical applications yet. If one has a broader view and focuses not only on the materials for the H-SOFCs, the electrode materials for the Li-ion batteries and H-SOFCs share some

* Corresponding author.
E-mail: lei.bi@usc.edu.cn, bilei81@gmail.com, bilei@vip.qq.com

common points. Many of these electrode materials are ceramic oxides and contain transition metals as their major compositions. Therefore, it would be reasonable to expect that some electrode materials for the Li-ion batteries could show decent performance for the H-SOFCs as well. More importantly, many of the electrode materials for the Li-ion batteries have been commercialized, and the application of the Li-ion battery electrode materials for the H-SOFCs could advance the development of the H-SOFCs.

In fact, some lithiated oxide cathodes have been used for the SOFCs, but only moderate performance has been achieved [20]. Very recently, $LiCo_{0.6}X_{0.4}O_2$ (X = Mn, Sr, and Zn) materials were applied as the cathodes for the H-SOFCs, and the optimal polarization resistance ($R_p$) is 0.55 $\Omega \cdot cm^2$ at 700 ℃ [21], which is inferior to the newly developed high-performing cathodes. These results imply that the traditional lithiated oxide cathodes might not be a good choice as the cathode candidate for the H-SOFCs. However, all of these have focused on using pure phase lithiated oxide cathodes and evaluated their suitability as the cathodes for the H-SOFCs. The lithiated oxide cathodes, such as the classical $LiCoO_2$, contain a large amount of Li element, and the Li element tends to evaporate during the synthesis procedure due to the high-temperature calcination. Therefore, an excess amount of Li should be added during the preparation process to compensate for the Li-evaporation and obtain the pure phase $LiCoO_2$ [22,23]. It is understandable that the Li loss could be detrimental to the performance of the Li-ion batteries, and the Li-evaporation has to be compensated [24]. However, the working mechanism of the H-SOFCs is different from that of the Li-ion batteries, which does not require the mobility of the Li-ions. It should be noted that the performance of the lithiated oxide cathodes for the H-SOFCs is reported to be only moderate [20,21], even though efforts are devoted to preparing the pure phase lithiated oxide cathodes. One may wonder about the performance of the lithiated oxide cathode for the H-SOFCs if the evaporated Li is not compensated, as no mobility of Li is needed in the H-SOFCs. Therefore, the classical Li-ion battery electrode $LiCoO_2$ was used in this study as the cathode for the H-SOFCs. The phase compositions for $LiCoO_2$ with and without the Li compensation were studied, and their performance for the H-SOFCs was investigated and compared, aiming to provide a new cathode system for the H-SOFCs.

## 2 Materials and method

$LiCoO_2$ was prepared by using $Li_2CO_3$ and $Co(NO_3)_3$ as starting materials [25]. $Li_2CO_3$ was dissolved in dilute nitric acid. According to Refs. [22,24], 4 mol% Li-excess was needed to compensate for the Li-evaporation during the synthesis to form the pure phase $LiCoO_2$. In contrast, the stoichiometric ratio of $Li_2CO_3$ and $Co(CO_3)_3$ was used in this study, making the molar ratio of Li∶Co keep at 1∶1 for the starting materials. In other words, no Li-excess was applied to compensate for the Li-evaporation during the synthesis procedure. The as-prepared powders were calcined at 850 ℃ for 3 h, followed by the phase examination using X-ray diffraction (XRD). The XRD was performed at a scanning rate of 3 (°)·$min^{-1}$ with Cu Kα radiation. The morphologies of the powders were characterized by scanning electron microscopy (SEM) and high-resolution transmission electron microscopy (HR-TEM). The stability of the powders was examined by treating the powders in both $CO_2$ and $H_2O$-containing atmospheres at a high temperature. The $CO_2$ and $H_2O$ concentrations were 20% and 30%, respectively. Then, the XRD was used to analyze the phase of the powders before and after the treatments.

To evaluate the efficiency of the $LiCoO_2$ cathodes for the H-SOFCs, the cathode slurry was deposited onto the electrolyte, and then being co-fired at 800 ℃ for 10 min. The electrolyte material used in this study was $BaCe_{0.7}Zr_{0.1}Y_{0.2}O_{3-\delta}$ (BCZY), and the anode was NiO–BCZY. The details for the preparations of the electrolyte powders and half-cells can be found in Ref. [26]. The single cells were tested by using humidified $H_2$ (3% $H_2O$) as the fuel. IV and electrochemical impedance spectroscopy (EIS) measurements were carried out by an electrochemical workstation (Squidstat Plus, Admiral Instrument) under open circuit voltage (OCV) condition. The frequency range was from 1 MHz to 0.1 Hz with an amplitude of 5 mV. The morphologies of the tested cells were observed by the SEM.

The first-principles calculation was carried out to investigate the $LiCoO_2$-based material, using density functional theory (DFT) method with Vienna *Ab-initio* Simulation Package (VASP) software. The calculation details can be found in Refs. [27–31].

## 3 Results and discussion

Figure 1(a) shows the XRD pattern for $LiCoO_2$ without Li-excess after being fired at 850 ℃ for 3 h. The $LiCoO_2$ powders with 4 mol% Li-excess were also prepared via the same procedure, and its XRD is shown in Fig. 1(a) as well. A pure phase is obtained with the $LiCoO_2$ powders with 4 mol% Li-excess. No other Li-related compounds, such as $Li_2O$ or $Li_2CO_3$, can be detected. This result suggests that the excess Li compensates for the Li-evaporation during the calcination procedure, agreeing with Ref. [24] that 4 mol% Li-excess is usually used to offset the Li-evaporation during the synthesis process, making $LiCoO_2$ achieve a pure phase. In contrast, if one looks at the XRD pattern of the $LiCoO_2$ powders without Li-excess, the main peaks correspond to the $LiCoO_2$ phase. However, some extra peaks corresponding to $Co_3O_4$ can be found, suggesting that the evaporation of Li in $LiCoO_2$ could lead to $Co_3O_4$ as the second phase if the Li-evaporation is not compensated by excess Li sources. Figure 1(b) shows the SEM image of the $LiCoO_2$ powders without Li-excess, and one can see that large sheet-like powders are $LiCoO_2$, and the small particles are $Co_3O_4$. The TEM image of the powders (Fig. 1(c)) shows a similar result that $LiCoO_2$ and $Co_3O_4$ form the

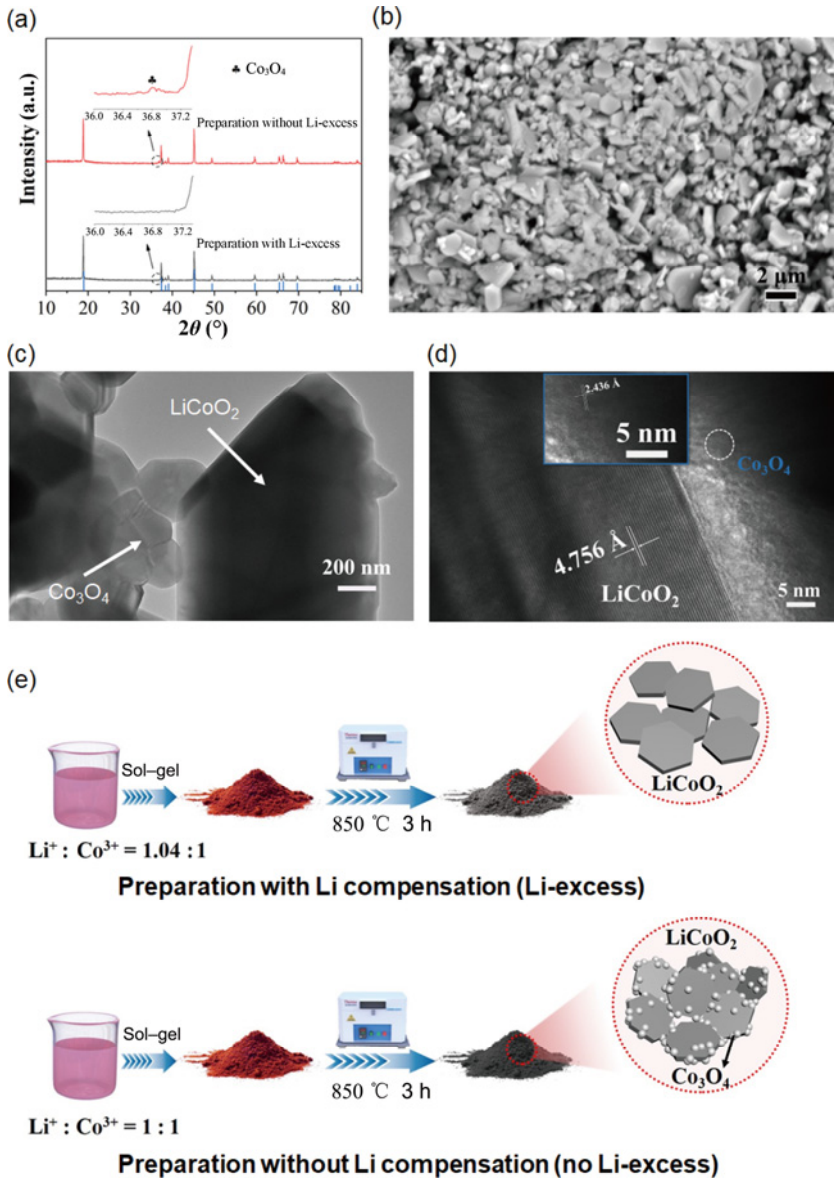


**Fig. 1** (a) XRD patterns for $LiCoO_2$ prepared with and without Li-excess to compensate Li-evaporation; (b) SEM, (c) TEM, and (d) HR-TEM images for $LiCoO_2$ powders without use of Li-excess ($LiCoO_2$+$Co_3O_4$), and (e) scheme for preparation of $LiCoO_2$ with and without use of Li-excess.

composite. The HR-TEM image shown in Fig. 1(d) presents the $LiCoO_2/Co_3O_4$ interface, indicating the *d*-spacing value of 4.756 Å corresponding to the (003) plane of $LiCoO_2$ and the *d*-spacing value of 2.436 Å corresponding to the (311) plane of $Co_3O_4$. To further demonstrate the formation of $Co_3O_4$ nanoparticles, additional SEM images were taken for $LiCoO_2$+$Co_3O_4$ (prepared by the exsolution of $Co_3O_4$ from $LiCoO_2$), $Co_3O_4$, and pure phase $LiCoO_2$ for analyzing the morphologies of these powders, and the results are shown in Fig. S1 in the Electronic Supplementary Material (ESM). One can see that $Co_3O_4$ are small nanoparticles, while the pure phase $LiCoO_2$ is a sheet-like shape. It is evident that the $LiCoO_2$+$Co_3O_4$ composite is the sheet-like $LiCoO_2$ surrounded by small $Co_3O_4$ nanoparticles. In addition, the elemental analysis (Fig. S2 in the ESM) indicates that these small nanoparticles only contain Co and O elements, confirming the formation of $Co_3O_4$. The C element detected as a carbon tape was used in the SEM observations, and the Au element detected as Au sputtering was used to increase the conductivity of the samples. Therefore, it can be concluded that the $LiCoO_2$ powders without Li-excess finally becomes the $LiCoO_2$+$Co_3O_4$ composite powders. Figure 1(e) shows the scheme of the $LiCoO_2$ powder preparation. After the sol–gel procedure, the precursor was calcined at 850 ℃ for 3 h. When there is excess Li, the Li-evaporation can be compensated with the production of the pure phase $LiCoO_2$. In contrast, when the stoichiometric ratio of Li and Co is used, no Li-excess is used, and thus no compensation of the Li-evaporation happens for the final product, leading to the formation of the $LiCoO_2$+$Co_3O_4$ composite. The compensation of Li to obtain the pure phase $LiCoO_2$ is understandable for the Li-ion batteries as the Li ions are required to move during the charge and discharge processes for the Li-ion batteries, and the deficiency in the Li content could lead to the reduced capacity of the batteries [32]. However, the Li-evaporation and the formation of $Co_3O_4$ might promote the cathode performance in the fuel cells as $Co_3O_4$ is reported to facilitate the oxygen reduction reaction (ORR) at the cathode for the SOFCs and improve the cathode performance [33]. Therefore, it is reasonable to expect that the $LiCoO_2$+$Co_3O_4$ composite could give a good performance for the H-SOFCs.

Figure 2(a) shows the IV and power density curves of a single H-SOFCs using the $LiCoO_2$+$Co_3O_4$ composite as the cathode. The cell's peak power densities (PPDs) are 1160, 896, and 603 $mW \cdot cm^{-2}$ at 700, 650, and 600 ℃, respectively. The PPDs tested at a temperature higher than 700 ℃ are not reported here, as obvious oxygen-ion conductions appear for proton-conducting oxides above 700 ℃ [4]. Figures 2(b)–2(d) show the cross-sectional view of the tested cell. A tri-layer structure can be observed, and the electrolyte layer contacts well with the cathode and anode. The fuel cell performance is much higher than those of the H-SOFCs using the traditional cathodes and comparable to or even higher than those of many H-SOFCs using recently developed cathodes, as indicated in Table 1 [34–42]. This result suggests that the $LiCoO_2$+$Co_3O_4$ composite is a high-performance cathode for the H-SOFCs.

The cell performance between the pure phase $LiCoO_2$ cathode and the $LiCoO_2$+$Co_3O_4$ cathode was further compared. Figure 3(a) shows the performance of the cell with the $LiCoO_2$ cathode and the $LiCoO_2$+$Co_3O_4$ cathode tested at 700 ℃. The PPD for the cell using the $LiCoO_2$ cathode is 879 $mW \cdot cm^{-2}$, and the PPD value increases to 1160 $mW \cdot cm^{-2}$ for the cell using the $LiCoO_2$+$Co_3O_4$ cathode under the same testing condition. The EIS analysis confirms that the *in-situ* formation of $Co_3O_4$ in the $LiCoO_2$ cathode is beneficial for the reduction of the $R_p$. One can see from Fig. 3(b) that the ohmic resistance ($R_{ohmic}$) is similar, being 0.148 and 0.141 $\Omega \cdot cm^2$ at 700 ℃ for the cells using the $LiCoO_2$ cathode and $LiCoO_2$+$Co_3O_4$ cathode, respectively. In contrast, an obvious difference in the $R_p$ can be observed. The $R_p$ for the pure phase $LiCoO_2$ cathode is 0.123 $\Omega \cdot cm^2$, and the $R_p$ value decreases to 0.043 $\Omega \cdot cm^2$ for the cell using the $LiCoO_2$+$Co_3O_4$ cathode under the same testing condition. The shrinkage in the $R_p$ is about 65% with the use of the $LiCoO_2$+$Co_3O_4$ cathode instead of the pure phase $LiCoO_2$ cathode. The $R_p$ for the $LiCoO_2$+$Co_3O_4$ cathode is even smaller than those for many recently reported cathodes for the H-SOFCs, as indicated in Table 1. It should be noted that only $LiCoO_2$ or $LiCoO_2$+$Co_3O_4$ was used as the cathode, and the $LiCoO_2$-based material was not mixed with the BCZY to form the composite cathode. The close $R_{ohmic}$ for both cells is expected because both cells are identically prepared except for the different cathodes used. In addition, the same Ni–BCZY anode is used for both cells, so the considerable gap in the $R_p$ should come from the cathode. The performance enhancement for the $LiCoO_2$+$Co_3O_4$ cathode is not only observed at 700 ℃ but also

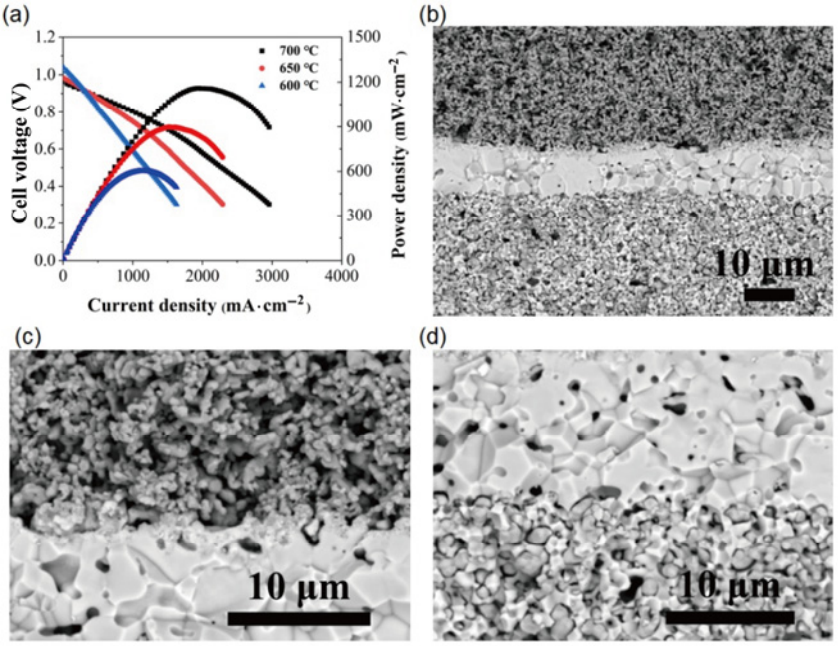


**Fig. 2** (a) Fuel cell performance for H-SOFCs using the $LiCoO_2$+$Co_3O_4$ cathode. Cross-sectional diagrams for (b) cell, (c) cathode/electrolyte, and (d) electrolyte/anode.

**Table 1 Comparison of performance of current $LiCoO_2$+$Co_3O_4$ cathode with other recently reported cathode materials for H-SOFCs**

| Cell configuration | Electrolyte thickness (μm) | Cathode composition | PPD (mW·cm$^{-2}$) | | | $R_p$ (700 ℃) (Ω·cm$^2$) | Year | Ref. |
|---|---|---|---|---|---|---|---|---|
| | | | 600 ℃ | 650 ℃ | 700 ℃ | | | |
| Ni–BCSF\|BCSF\|F–BCSF | 15 | $Ba_{0.5}Sr_{0.5}Co_{0.8}Fe_{0.2}O_{2.9-\delta}F_{0.1}$ | 260 | — | 480 | — | 2018 | [34] |
| Ni–BCZY\|BCZY\|LSN | 15 | $La_{1.2}Sr_{0.8}NiO_4$ | 223 | 330 | 461 | 0.26 | 2018 | [35] |
| Ni–BZCYYb\|BZCYYb\|NBSCCF–BCZYYb | 13 | $Nd(Ba_{0.4}Sr_{0.4}Ca_{0.2})Co_{1.6}Fe_{0.4}O_{5+\delta}$ | 217 | 501 | 776 | 0.114 | 2019 | [36] |
| Ni–BCZY5\|BCZY5\|CC | 25 | $Ca_3Co_4O_{9+\delta}$ | 150 | 220 | 290 | 0.12 | 2019 | [37] |
| Ni–BCZY\|BCZY\|BSSNC | 32 | $Ba_{0.5}Sr_{0.5}Sc_{0.175}Nb_{0.025}Co_{0.8}O_{3-\delta}$ | — | — | 633 | 0.17 | 2019 | [38] |
| Ni–BCZYYb\|BCZYYb\|SFMZ | 20 | $Sr_2Fe_{1.5}Mo_{0.4}Zr_{0.1}O_{6-\delta}$ | — | 630 | 790 | 0.169 | 2020 | [39] |
| Ni–BCZYYb\|BCZYYb\|PrBaNiMn | 12 | $Pr_2BaNiMnO_{7-\delta}$ | 570 | 776 | 1070 | 0.084 | 2020 | [40] |
| Ni–BCZY\|BCZY\|LSCF–BCZY | 25 | $La_{0.6}Sr_{0.4}Co_{0.2}Fe_{0.8}O_{3-\delta}$ | 465 | — | — | — | 2021 | [41] |
| Ni–BCZY\|BCZY\|LSFN | 30 | $La_{0.25}Sr_{2.75}FeNiO_{7-\delta}$ | 219 | 348 | — | — | 2021 | [42] |
| Ni–BCZY\|BCZY\|LCO–$Co_3O_4$ | 12 | $LiCoO_2$–$Co_3O_4$ | 603 | 896 | 1160 | 0.043 | 2022 | This work |

Note: BCSF is $BaCe_{0.8}Sm_{0.2}F_{0.1}O_{2.85}$, LSN is $La_{1.2}Sr_{0.8}NiO_4$, BCZY5 is $BaCe_{0.5}Zr_{0.3}Y_{0.2}O_{3-\delta}$, BCZYYb is $BaZr_{0.1}Ce_{0.7}Y_{0.1}Yb_{0.1}O_{3-\delta}$, NBSCCF is $Nd(Ba_{0.4}Sr_{0.4}Ca_{0.2})Co_{1.6}Fe_{0.4}O_{5+\delta}$; CC is $Ca_3Co_4O_{9+\delta}$, BSSNC is $Ba_{0.5}Sr_{0.5}Sc_{0.175}Nb_{0.025}Co_{0.8}O_{3-\delta}$, SFMZ is $Sr_2Fe_{1.5}Mo_{0.4}Zr_{0.1}O_{6-\delta}$, LSCF is $La_{0.6}Sr_{0.4}Co_{0.2}Fe_{0.8}O_{3-\delta}$, LSFN is $La_{0.25}Sr_{2.75}FeNiO_{7-\delta}$, and LCO is $LiCoO_2$.

detected at other testing temperatures. Figures 3(c) and 3(d) show the $R_{ohmic}$ and $R_p$ measured at different testing temperatures, respectively. It is found that the $R_{ohmic}$ is similar for both cells tested at different temperatures, but the $R_p$ shows apparent differences. As a result, the performance of the $LiCoO_2$+$Co_3O_4$ cathode cell is evidently higher than that of the cell using the pure phase $LiCoO_2$ cathode, as shown in Fig. 3(e). This result suggests that the difference in the $R_p$ rather than the $R_{ohmic}$ leads to a significant difference in the cell performance for the $LiCoO_2$+$Co_3O_4$ cell and the $LiCoO_2$ cell. The use of $LiCoO_2$+$Co_3O_4$ cathode significantly improves the cathode performance and the fuel cell performance. Although the evaporation of Li in $LiCoO_2$ is not desirable for the Li-ion batteries, the Li-evaporation in $LiCoO_2$ and the subsequently formed $Co_3O_4$ second phase benefit its application in the H-SOFCs, leading to higher fuel cell performance and lower $R_p$ compared with the pure phase $LiCoO_2$ electrode. Not only is the higher performance for the

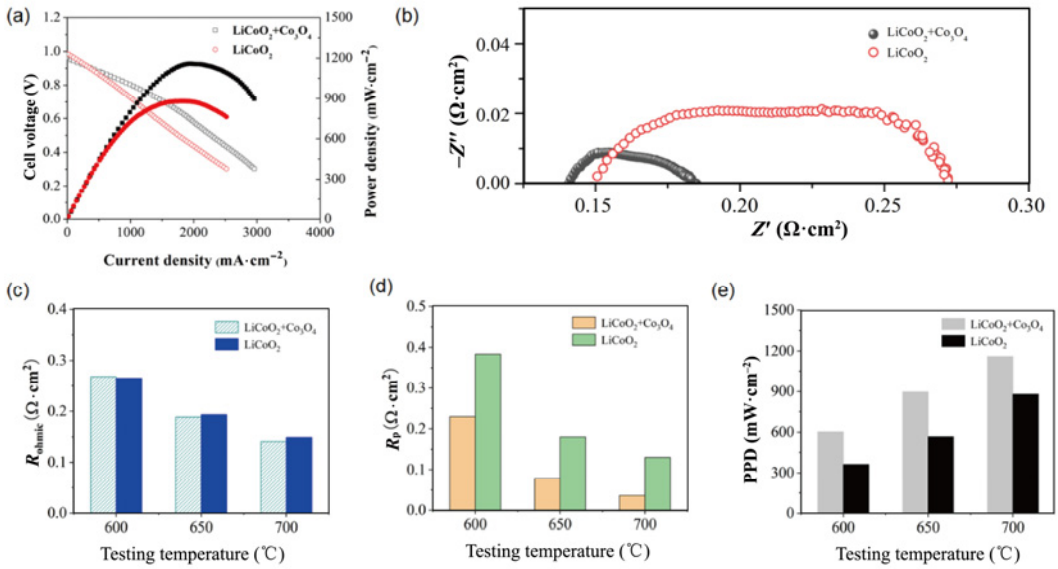


**Fig. 3** Comparison of (a) fuel cell performance and (b) EIS for the H-SOFCs using $LiCoO_2$+$Co_3O_4$ and $LiCoO_2$ cathodes tested at 700 ℃; comparison of (c) $R_{ohmic}$, (d) $R_p$, and (e) PPDs for cells using $LiCoO_2$+$Co_3O_4$ and $LiCoO_2$ cathodes tested from 600 to 700 ℃.

$LiCoO_2$+$Co_3O_4$ cathode compared with that for the pure phase $LiCoO_2$ cathode in this study, but also the $R_p$ of the current $LiCoO_2$+$Co_3O_4$ cathode is one or two orders of magnitude smaller than that of the lithiated oxide cathodes for the H-SOFCs reported in Ref. [21], which is 0.55 to a few Ω·cm$^2$ at 700 ℃, even though the studies on the lithiated oxide cathodes for the H-SOFCs are very scarce. This result suggests that the *in-situ* formation of $Co_3O_4$ could dramatically improve the cathode performance and may bring a new life to the lithiated oxide cathodes for the H-SOFCs. It should be mentioned that further reducing the Li content does not further improve the cell performance. We have also synthesized the $Li_{0.95}CoO_2$ material, in which the Li content is further reduced, to check whether further reducing the Li content can further increase or decrease the cell performance. The fuel cell performance with the $Li_{0.95}CoO_2$ cathode is shown in Fig. S3 in the ESM. The cell's PPDs are 1002, 657, and 422 mW·cm$^{-2}$ at 700, 650, and 600 ℃, respectively. Although the performance is still larger than that of the fuel cell using the pure phase $LiCoO_2$, the performance is reduced compared with that of the $LiCoO_2$+$Co_3O_4$ composite reported above.

The DFT calculations were performed to give insights into the high performance of the $LiCoO_2$+$Co_3O_4$ cathode. The formation of oxygen vacancies ($V_O$) is critical for the cathode performance as it dramatically influences the ORR activity of the cathode [43] and the oxygen-ion diffusions [44]. The Li-evaporation could lead to the loss of $Li^+$, and extra oxygen vacancies are formed for the charge compensation. The defect reaction can be written as $2Li_{Li} \rightarrow 2V'_{Li} + V_O^{\bullet\bullet}$, where $V'_{Li}$ represents the Li vacancy due to the Li-evaporation, and $V_O^{\bullet\bullet}$ is the oxygen vacancy. In addition, the formation of $V_O$ is the pre-factor for the protonation according to the reaction $H_2O + V_O^{\bullet\bullet} + O_O^{\times} \Leftrightarrow 2OH^{\bullet}$, where $O_O^{\times}$ means the lattice oxygen, and $OH^{\bullet}$ means the proton defect, which is another crucial parameter for the cathode of H-SOFCs [45]. Therefore, the formation energies of $V_O$ ($E_{V_O}$) for the pure phase $LiCoO_2$ and $LiCoO_2$/$Co_3O_4$ are calculated. The $E_{V_O}$ was calculated according to $E_{V_O} = E_{defect} + \frac{1}{2}E_{O_2} - E_{perfect}$ [29], where $E_{defect}$ is the total energy of defective bulk, $E_{O_2}$ is the energy of molecular oxygen, and $E_{perfect}$ is the total energy of the perfect bulk. The $E_{V_O}$ for $LiCoO_2$ is calculated to be 3.76 eV, which is relatively large compared with those for other cathode materials for the SOFCs. This result indicates that the $V_O$ formation in the pure phase $LiCoO_2$ has to overcome a high energy barrier. This result could explain that the reported lithiated oxide cathodes only show moderate performance for the SOFCs. When the $LiCoO_2$ material is prepared without an excess of Li, the final product is the $LiCoO_2$+$Co_3O_4$ composite, and Fig. 4(a) shows the DFT-calculated configuration of the $LiCoO_2$/$Co_3O_4$ supercell. Both the

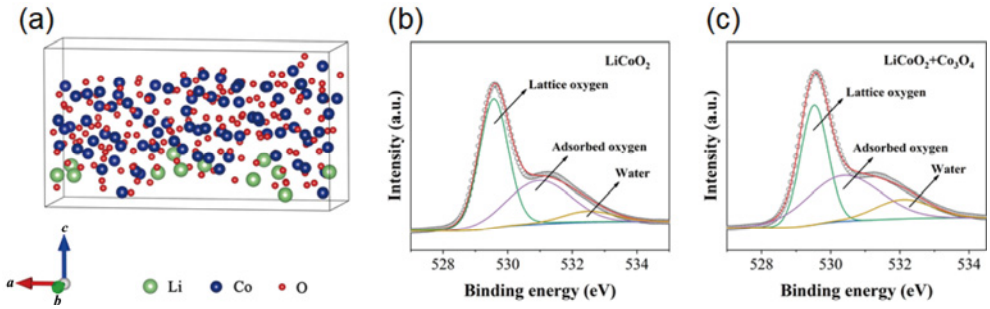


**Fig. 4** (a) DFT-calculated configuration for $LiCoO_2/Co_3O_4$ structure. XPS O 1s curves for (b) $LiCoO_2$ and (c) $LiCoO_2$+$Co_3O_4$.

bulks of $LiCoO_2$ and $Co_3O_4$ are calculated for structural optimizations. Then, the (104) surface of $LiCoO_2$ and the (110) surface of $Co_3O_4$ are cleaved for the combination. The (104) surface used for $LiCoO_2$ and the (110) surface used for $Co_3O_4$ are based on the previous reports as they are the most exposed surface for $LiCoO_2$ [46,47] and $Co_3O_4$ [48,49]. The supercell of the $LiCoO_2$ and $Co_3O_4$ surfaces are expanded to make a similar lattice constant between $LiCoO_2$ and $Co_3O_4$, and then the combination can be obtained. The final supercell for the $LiCoO_2/Co_3O_4$ contains 216 atoms. There are a certain number of $LiCoO_2/Co_3O_4$ interfaces. For the $LiCoO_2/Co_3O_4$ interface, we have performed the $E_{V_O}$ calculation at both $LiCoO_2$ and $Co_3O_4$ sides, and found that the $E_{V_O}$ at the $LiCoO_2$ side has the lowest energy, which means that the $V_O$ is more favourable to form at the $LiCoO_2$ side. The $E_{V_O}$ at the $LiCoO_2/Co_3O_4$ interface is calculated to be 0.46 eV, which is about one order of magnitude lower than that at the pure phase $LiCoO_2$, indicating that the $V_O$ formation is thermodynamically more favourable with the appearance of $Co_3O_4$. The oxygen species of $LiCoO_2$ and $LiCoO_2$+ $Co_3O_4$ are investigated by X-ray photoelectron spectroscopy (XPS), and the results are shown in Figs. 4(b) and 4(c), respectively. The ratio between the adsorbed oxygen and the lattice oxygen reflects the $V_O$ content [50,51], and the ratio is 0.69 and 1.02 for $LiCoO_2$ and $LiCoO_2$+ $Co_3O_4$, respectively, suggesting that the $V_O$ content in $LiCoO_2$+$Co_3O_4$ is higher than that in the pure phase $LiCoO_2$ that agrees with the DFT calculation results. The iodometric titration method was further used to measure the oxygen vacancy content in $LiCoO_2$ and $LiCoO_2$+$Co_3O_4$. It is found that the oxygen vacancy concentration in the pure phase $LiCoO_2$ is 0.13, and the value increases to 0.22 for the $LiCoO_2$+$Co_3O_4$ composite, suggesting an increase in the oxygen vacancies for $LiCoO_2$+$Co_3O_4$ compared with those for the pure phase $LiCoO_2$. The result is consistent with the DFT calculations and XPS analysis.

In addition, the distance between Co 3d and O 2p in $LiCoO_2$+$Co_3O_4$ is reduced compared with that in the pure phase $LiCoO_2$. Figures 5(a) and 5(b) show density of states (DOS) for Co 3d and O 2p orbitals for $LiCoO_2$ and $LiCoO_2$+$Co_3O_4$, respectively. The distance between Co 3d and O 2p is 3.17 for the pure phase $LiCoO_2$, and the value decreases to 2.86 with the appearance of $Co_3O_4$ for $LiCoO_2$+$Co_3O_4$. The reduced distance between Co 3d and O 2p is associated with enhanced charge transfer, thereby benefiting the ORR [52]. Therefore, the $LiCoO_2$+$Co_3O_4$ cathode performs better compared to the pure phase $LiCoO_2$.

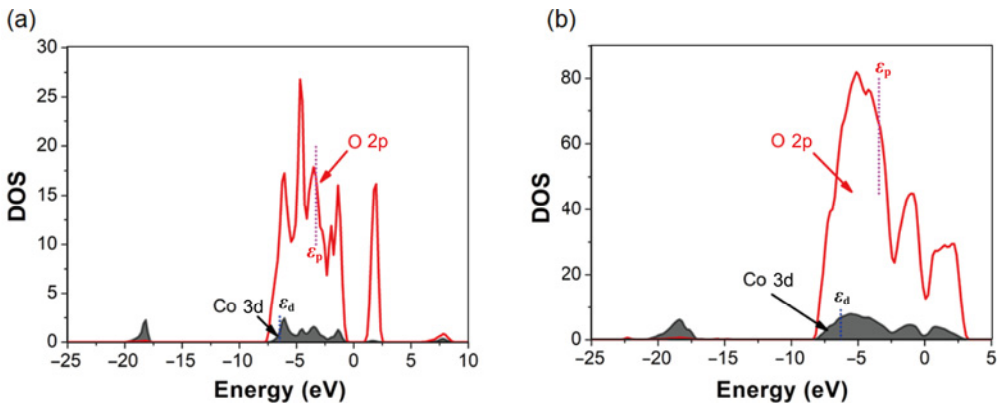


**Fig. 5** DFT-calculated DOS of Co 3d and O 2p orbitals in (a) $LiCoO_2$ and (b) $LiCoO_2$+$Co_3O_4$, where $\varepsilon_p$ means the p-band center for O 2p, and $\varepsilon_d$ means the d-band center for Co 3d.

As the cathode for the H-SOFCs, another primary concern is the stability of the material, as this parameter is essential for its potential practical applications. The $LiCoO_2$+$Co_3O_4$ composite was treated in the $CO_2$-containing atmosphere at 600 ℃, and the result is shown in Fig. 6(a). One can see that there is no extra peak under the treatment of 12 h, suggesting that the $LiCoO_2$+$Co_3O_4$ composite has good chemical stability against $CO_2$. The good chemical stability of the $LiCoO_2$+$Co_3O_4$ composite can be expected that no high-basicity element (such as Ba) is involved in the material, restricting its reaction with acid gases (such as $CO_2$). The $LiCoO_2$+$Co_3O_4$ composite also presents good chemical stability against steam. The composite powders were treated in a 30% $H_2O$-containing air atmosphere at 600 ℃ for 10 h. Figure 6(b) shows the XRD patterns for the $LiCoO_2$+$Co_3O_4$ composite before and after the treatment. The XRD pattern remains unchanged after the treatment, suggesting that there is no evident reaction between the $LiCoO_2$+$Co_3O_4$ composite and $H_2O$, thus demonstrating its excellent stability against $H_2O$ at high temperatures. If we enlarge the XRD patterns before and after the treatment, one can see that the XRD peak slightly shifts to a lower angle after the treatment (Fig. S4 in the ESM), suggesting the expansion of the lattice. This phenomenon is also reported in Ref. [53], which is due to the adsorption of water in the lattice of the material. Although the peak shift is not very profound because the powders are treated at 600 ℃, and the hydration degree decreases with the increasing temperatures [54], the peak shift can still be observed. The excellent chemical stability of the $LiCoO_2$+$Co_3O_4$ composite also leads to good fuel cell stability under the operation condition. Figure 6(c) shows the stability test result for the fuel cell. The cell works in a stable way for more than 500 h, suggesting that the $LiCoO_2$+$Co_3O_4$ composite provides high performance for the H-SOFCs and integrates the stability of the single-cell well.

## 4 Conclusions

In this study, we took advantage of the Li-evaporation in $LiCoO_2$ to form the $LiCoO_2$+$Co_3O_4$ composite as a cathode for the H-SOFCs. The Li-evaporation in $LiCoO_2$ was regarded as a drawback for the Li-ion batteries that required excess Li in the preparation procedure for the compensation. However, $LiCoO_2$ without the Li compensation turned out to be the $LiCoO_2$+$Co_3O_4$ composite after the calcination, which was applied as the cathode for the H-SOFCs. The $LiCoO_2$+$Co_3O_4$ composite generated higher fuel cell performance and lower $R_p$ for the H-SOFCs compared with the pure phase $LiCoO_2$ cathode. The DFT calculations coupled with experiments indicated that the appearance of $Co_3O_4$ due to the Li-evaporation in $LiCoO_2$ was beneficial to the formation of the oxygen vacancies, facilitating the cathode reactions. The improved oxygen vacancy content and the enhanced catalytic activity induced by the formation of the $Co_3O_4$ nanoparticles contribute to better cathode performance and larger fuel cell output. In addition, the high electrochemical performance of $LiCoO_2$+$Co_3O_4$ for the H-SOFCs did not impair its stability. The $LiCoO_2$+$Co_3O_4$ composite presented excellent stability in both $CO_2$ and $H_2O$. In addition, the good stability of the single-cell using the $LiCoO_2$+$Co_3O_4$ cathode under the working condition was also demonstrated, suggesting that $LiCoO_2$+$Co_3O_4$ composite integrated both high performance and good stability. This study bridges the electrode materials between the Li-ion batteries and the H-SOFCs and indicates that the disadvantageous feature in the Li-ion batteries may

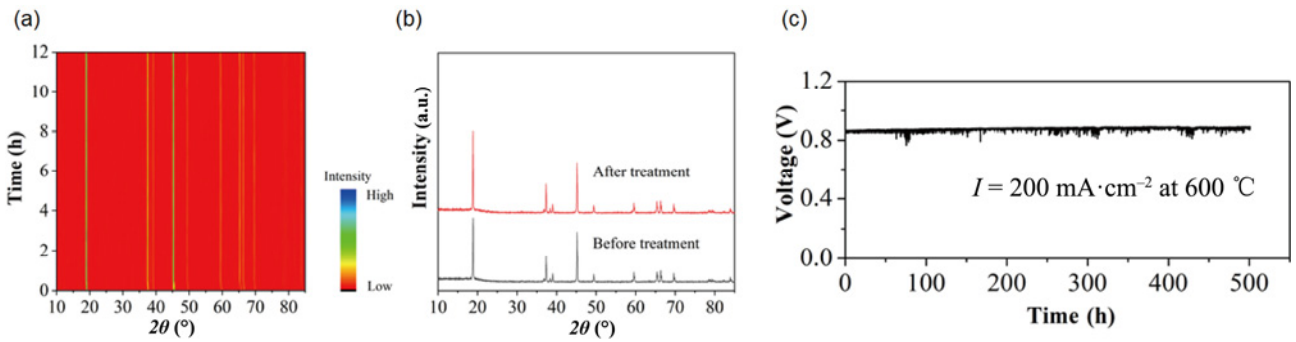


**Fig. 6** (a) Time-course XRD patterns for $LiCoO_2$+$Co_3O_4$ composite measured by *in-situ* XRD at 600 ℃ in a $CO_2$-containing atmosphere; (b) XRD patterns for $LiCoO_2$+$Co_3O_4$ composite before and after the treatment in wet air (30% $H_2O$); (c) stability test for H-SOFCs using $LiCoO_2$+$Co_3O_4$ cathode.

become an advantage for the H-SOFCs, probably opening a new area of cathode design for the H-SOFCs.

## Acknowledgements

This work was supported by the National Natural Science Foundation of China (Grant No. 51972183), the Hundred Youth Talents Program of Hunan, and the Startup Funding for Talents at University of South China.

## Declaration of competing interest

The authors have no competing interests to declare that are relevant to the content of this article.

## Electronic Supplementary Material

Supplementary material is available in the online version of this article at https://doi.org/10.1007/s40145-022-0651-x.

## References

[1] Zhang YW, Mei J, Yan C, *et al*. Bioinspired 2D nanomaterials for sustainable applications. *Adv Mater* 2020, **32**: 1902806.

[2] Sun ZQ, Liao T, Li WX, *et al*. Beyond seashells: Bioinspired 2D photonic and photoelectronic devices. *Adv Funct Mater* 2019, **29**: 1901460.

[3] Dai HL, Yin YR, Li XM, *et al*. A new Sc-doped $La_{0.5}Sr_{0.5}MnO_{3-\delta}$ cathode allows high performance for proton-conducting solid oxide fuel cells. *Sustain Mater Techno* 2022, **32**: e00409.

[4] Iwahara H. Oxide-ionic and protonic conductors based on perovskite-type oxides and their possible applications. *Solid State Ionics* 1992, **52**: 99–104.

[5] Ling JR, Zhou YF, Xu WT, *et al*. Red-emitting YAG:Ce, Mn transparent ceramics for warm WLEDs application. *J Adv Ceram* 2020, **9**: 45–54.

[6] Zhang Y, Chen B, Guan DQ, *et al*. Thermal-expansion offset for high-performance fuel cell cathodes. *Nature* 2021, **591**: 246–251.

[7] Zhang Y, Knibbe R, Sunarso J, *et al*. Recent progress on advanced materials for solid-oxide fuel cells operating below 500 ℃. *Adv Mater* 2017, **29**: 1700132.

[8] Liang MZ, He F, Zhou C, *et al*. Nickel-doped $BaCo_{0.4}Fe_{0.4}Zr_{0.1}Y_{0.1}O_{3-\delta}$ as a new high-performance cathode for both oxygen-ion and proton conducting fuel cells. *Chem Eng J* 2021, **420**: 127717.

[9] Wu S, Xu X, Li XM, *et al*. High-performance proton-conducting solid oxide fuel cells using the first-generation Sr-doped $LaMnO_3$ cathode tailored with Zn ions. *Sci China Mater* 2022, **65**: 675–682.

[10] Zvonareva I, Fu XZ, Medvedev D, *et al*. Electrochemistry and energy conversion features of protonic ceramic cells with mixed ionic-electronic electrolytes. *Energ Environ Sci* 2022, **15**: 439–465.

[11] Xie D, Li K, Yang J, *et al*. High-performance $La_{0.5}(Ba_{0.75}Ca_{0.25})_{0.5}Co_{0.8}Fe_{0.2}O_{3-\delta}$ cathode for proton-conducting solid oxide fuel cells. *Int J Hydrogen Energ* 2021, **46**: 10007–10014.

[12] Chen M, Xie XB, Guo JH, *et al*. Space charge layer effect at the platinum anode/$BaZr_{0.9}Y_{0.1}O_{3-\delta}$ electrolyte interface in proton ceramic fuel cells. *J Mater Chem A* 2020, **8**: 12566–12575.

[13] Chen M, Chen DC, Wang K, *et al*. Densification and electrical conducting behavior of $BaZr_{0.9}Y_{0.1}O_{3-\delta}$ proton conducting ceramics with NiO additive. *J Alloys Compd* 2019, **781**: 857–865.

[14] Li J, Wang C, Wang XF, *et al*. Sintering aids for proton-conducting oxides—A double-edged sword? A mini review. *Electrochem Commun* 2020, **112**: 106672.

[15] Tian HC, Li WY, Ma L, *et al*. Deconvolution of water-splitting on the triple-conducting Ruddlesden–Popper-phase anode for protonic ceramic electrolysis cells. *ACS Appl Mater Interfaces* 2020, **12**: 49574–49585.

[16] Yin YR, Yu SF, Dai HL, *et al*. Triggering interfacial activity of the traditional $La_{0.5}Sr_{0.5}MnO_3$ cathode with Co-doping for proton-conducting solid oxide fuel cells. *J Mater Chem A* 2022, **10**: 1726–1734.

[17] Zhang LL, Yin YR, Xu YS, *et al*. Tailoring $Sr_2Fe_{1.5}Mo_{0.5}O_{6-\delta}$ with Sc as a new single-phase cathode for proton-conducting solid oxide fuel cells. *Sci China Mater* 2022, **65**: 1485–1494.

[18] Tarutin AP, Lyagaeva JG, Medvedev DA, *et al*. Recent advances in layered $Ln_2NiO_{4+\delta}$ nickelates: Fundamentals and prospects of their applications in protonic ceramic fuel and electrolysis cells. *J Mater Chem A* 2021, **9**: 154–195.

[19] Song YF, Chen YB, Wang W, *et al*. Self-assembled triple-conducting nanocomposite as a superior protonic ceramic fuel cell cathode. *Joule* 2019, **3**: 2842–2853.

[20] Zhang L, Lan R, Kraft A, *et al*. Cost-effective solid oxide fuel cell prepared by single step co-press–firing process with lithiated NiO cathode. *Electrochem Commun* 2010, **12**: 1589–1592.

[21] Yusoff WNAW, Somalu MR, Baharuddin NA, *et al*. Enhanced performance of lithiated cathode materials of $LiCo_{0.6}X_{0.4}O_2$ (X = Mn, Sr, Zn) for proton-conducting solid oxide fuel cell applications. *Int J Energ Res* 2020, **44**: 11783–11793.

[22] Predoana L, Jitianu A, Voicescu M, *et al*. Study of formation of $LiCoO_2$ using a modified Pechini aqueous sol–gel process. *J Sol–Gel Sci Techn* 2015, **74**: 406–418.

[23] Li L, Chen RJ, Zhang XX, *et al*. Preparation and electrochemical properties of re-synthesized $LiCoO_2$ from spent lithium-ion batteries. *Chinese Sci Bull* 2012, **57**: 4188–4194.

[24] Han SJ, Xia YG, Wei Z, *et al*. A comparative study on the oxidation state of lattice oxygen among $Li_{1.14}Ni_{0.136}Co_{0.136}Mn_{0.544}O_2$, $Li_2MnO_3$, $LiNi_{0.5}Co_{0.2}Mn_{0.3}O_2$ and $LiCoO_2$ for

the initial charge–discharge. *J Mater Chem A* 2015, **3**: 11930–11939.

[25] Xu X, Bi L, Zhao XS. Highly-conductive proton-conducting electrolyte membranes with a low sintering temperature for solid oxide fuel cells. *J Membrane Sci* 2018, **558**: 17–25.

[26] Xu X, Xu YS, Ma JM, *et al*. Tailoring electronic structure of perovskite cathode for proton-conducting solid oxide fuel cells with high performance. *J Power Sources* 2021, **489**: 229486.

[27] Xu X, Wang HQ, Fronzi M, *et al*. Tailoring cations in a perovskite cathode for proton-conducting solid oxide fuel cells with high performance. *J Mater Chem A* 2019, **7**: 20624–20632.

[28] Tao ZR, Xu X, Bi L. Density functional theory calculations for cathode materials of proton-conducting solid oxide fuel cells: A mini-review. *Electrochem Commun* 2021, **129**: 107072.

[29] Munoz-Garcia AB, Tuccillo M, Pavone M. Computational design of cobalt-free mixed proton–electron conductors for solid oxide electrochemical cells. *J Mater Chem A* 2017, **5**: 11825–11833.

[30] Yin YR, Dai HL, Yu SF, *et al*. Tailoring cobalt-free $La_{0.5}Sr_{0.5}FeO_{3-\delta}$ cathode with a nonmetal cation-doping strategy for high-performance proton-conducting solid oxide fuel cells. *SusMat* 2022, https://doi.org/10.1002/sus2.79.

[31] Xu YS, Xu X, Bi L. A high-entropy spinel ceramic oxide as the cathode for proton-conducting solid oxide fuel cells. *J Adv Ceram* 2022, **11**: 794–804.

[32] Mei J, Liao T, Liang J, *et al*. Toward promising cathode catalysts for nonlithium metal–oxygen batteries. *Adv Energy Mater* 2020, **10**: 1901997.

[33] Zhang HZ, Yang WS. Highly efficient electrocatalysts for oxygen reduction reaction. *Chem Commun* 2007: 4215–4217.

[34] Xie Y, Shi N, Huan DM, *et al*. A stable and efficient cathode for fluorine-containing proton-conducting solid oxide fuel cells. *ChemSusChem* 2018, **11**: 3423–3430.

[35] Yang SJ, Wen YB, Zhang JC, *et al*. Electrochemical performance and stability of cobalt-free $Ln_{1.2}Sr_{0.8}NiO_4$ (Ln = La and Pr) air electrodes for proton-conducting reversible solid oxide cells. *Electrochim Acta* 2018, **267**: 269–277.

[36] Chen JY, Li J, Jia LC, *et al*. A novel layered perovskite $Nd(Ba_{0.4}Sr_{0.4}Ca_{0.2})Co_{1.6}Fe_{0.4}O_{5+\delta}$ as cathode for proton-conducting solid oxide fuel cells. *J Power Sources* 2019, **428**: 13–19.

[37] Pikalova E, Kolchugin A, Koroleva M, *et al*. Functionality of an oxygen $Ca_3Co_4O_{9+\delta}$ electrode for reversible solid oxide electrochemical cells based on proton-conducting electrolytes. *J Power Sources* 2019, **438**: 226996.

[38] Zhang YD, Zhu AK, Guo YM, *et al*. Electrochemical performance and effect of moisture on $Ba_{0.5}Sr_{0.5}Sc_{0.175}Nb_{0.025}Co_{0.8}O_{3-\delta}$ oxide as a promising electrode for proton-conducting solid oxide fuel cells. *Appl Energ* 2019, **238**: 344–350.

[39] Ren RZ, Wang ZH, Meng XG, *et al*. Tailoring the oxygen vacancy to achieve fast intrinsic proton transport in a perovskite cathode for protonic ceramic fuel cells. *ACS Appl Energ Mater* 2020, **3**: 4914–4922.

[40] Wang Q, Hou J, Fan Y, *et al*. $Pr_2BaNiMnO_{7-\delta}$ double-layered Ruddlesden–Popper perovskite oxides as efficient cathode electrocatalysts for low temperature proton conducting solid oxide fuel cells. *J Mater Chem A* 2020, **8**: 7704–7712.

[41] Cao D, Zhou MY, Yan XM, *et al*. High performance low-temperature tubular protonic ceramic fuel cells based on barium cerate–zirconate electrolyte. *Electrochem Commun* 2021, **125**: 106986.

[42] Ling YH, Guo TM, Guo YY, *et al*. New two-layer Ruddlesden–Popper cathode materials for protonic ceramics fuel cells. *J Adv Ceram* 2021, **10**: 1052–1060.

[43] Xie D, Ling A, Yan D, *et al*. A comparative study on the composite cathodes with proton conductor and oxygen ion conductor for proton-conducting solid oxide fuel cell. *Electrochim Acta* 2020, **344**: 136143.

[44] Kilner JA, Burriel M. Materials for intermediate-temperature solid-oxide fuel cells. *Annu Rev Mater Res* 2014, **44**: 365–393.

[45] Duan CC, Huang J, Sullivan N, *et al*. Proton-conducting oxides for energy conversion and storage. *Appl Phys Rev* 2020, **7**: 011314.

[46] Boev AO, Fedotov SS, Abakumov AM, *et al*. The role of antisite defect pairs in surface reconstruction of layered $AMO_2$ oxides: A DFT+U study. *Appl Surf Sci* 2021, **537**: 147750.

[47] Vallverdu G, Minvielle M, Andreu N, *et al*. First principle study of the surface reactivity of layered lithium oxides $LiMO_2$ (M = Ni, Mn, Co). *Surf Sci* 2016, **649**: 46–55.

[48] Liu L, Xiao Y. Theoretical exploration electrocatalytic active of spinel $M_2CoO_4$ (M = Co, Fe and Ni) as efficient catalyst for water splitting. *Comp Mater Sci* 2021, **187**: 110082.

[49] Liu Q, Yu B, Liao XB, *et al*. Facet-dependent oxygen reduction reaction activity on the surfaces of $Co_3O_4$. *Energy Environ Mater* 2021, **4**: 407–412.

[50] Zhang XH, Pei CL, Chang X, *et al*. $FeO_6$ octahedral distortion activates lattice oxygen in perovskite ferrite for methane partial oxidation coupled with $CO_2$ splitting. *J Am Chem Soc* 2020, **142**: 11540–11549.

[51] Xu YS, Liu XH, Cao N, *et al*. Defect engineering for electrocatalytic nitrogen reduction reaction at ambient conditions. *Sustain Mater Techno* 2021, **27**: e00229.

[52] Zhou MZ, Liu JP, Ye YJ, *et al*. Enhancing the intrinsic activity and stability of perovskite cobaltite at elevated temperature through surface stress. *Small* 2021, **17**: 2104144.

[53] Ding HP, Wu W, Jiang C, *et al*. Self-sustainable protonic ceramic electrochemical cells using a triple conducting electrode for hydrogen and power production. *Nat Commun* 2020, **11**: 1907.

[54] Fabbri E, Pergolesi D, Licoccia S, *et al*. Does the increase in Y-dopant concentration improve the proton conductivity of $BaZr_{1-x}Y_xO_{3-\delta}$ fuel cell electrolytes? *Solid State Ionics* 2010, **181**: 1043–1051.